VERTICAL DYNAMICS OF THE ENERGY RELEASE PROCESS IN A SIMPLE TWO-RIBBON FLARE

BOJAN VRŠNAK[1], KARL-LUDWIG KLEIN[2], ALEXANDER WARMUTH[3], WOLFGANG OTRUBA[4] and MARINA SKENDER[5]

[1]*Hvar Observatory, Faculty of Geodesy, Kačićeva 26, 10000 Zagreb, Croatia (e-mail: bvrsnak@geodet.geof.hr)*

[2]*Observatoire de Paris, Section de Meudon, LESIA, CNRS-FRE 2461, F-92195 Meudon, France (e-mail: Ludwig.klein@obspm.fr)*

[3]*Astrophysikalisches Institut Potsdam, An der Sternwarte 16, D-14482 Potsdam, Germany (e-mail: awarmuth@aip.de)*

[4]*Kanzelhöhe Solar Observatory, 9521 Treffen, Austria (e-mail: otruba@solobskh.ac.at)*

[5] *Rudjer Bošković Institute, Bijenička 54, HR-10000 Zagreb, Croatia (e-mail: marina@rudjer.irb.hr)*

(Received 27 December 2002; accepted 19 February 2003)

Abstract. Observations of the quiescent filament eruption and the spotless two-ribbon flare of 12 September 2000 are presented. A simple flare morphology, large spatial scales, and a suitable viewing angle provide insight into characteristics of the energy release process which is attributed to the reconnection process in the current sheet formed below the eruptive filament. The flare ribbons appeared and started to expand laterally while the filament was still recognizable, enabling simultaneous measurements of the ribbon separation w and the height of the lower edge of the filament, h. The ratio w/h estimated for the expanding portions of ribbons indicates that the width-to-length ratio of the current sheet at the onset of the fast reconnection ranges between $\frac{1}{18}$ and $\frac{1}{9}$. The ribbon elements characterized by $w/h > \frac{1}{6}$ remained stationary. The Nançay radioheliograph data in the decimeter–meter wavelengths show one group of radio bursts ahead of the filament (moving type IV burst) and another group behind the filament. The centroids of the radio sources behind the filament were confined to the region outlined by the lower edge of the filament and the magnetic inversion line, suggestive of emission from the current sheet. Sources were preferably located close to the lower edge of the filament and some appeared close to the magnetic inversion line. Two possible explanations are discussed: one in terms of the fast-mode bow shocks in the reconnection outflow jets, and another in terms of a multiple tearing of the current sheet and subsequent coalescence of plasmoids.

1. Introduction

Eruptive prominences are frequently accompanied by two-ribbon flares, sometimes also called dynamical flares (Švestka, 1976). Such flares are characterized by the formation and lateral expansion of two bright chromospheric ribbons aligned with the inversion line of the photospheric magnetic field (the 'neutral line'). The ribbons are connected by an arcade of hot, soft X-ray emitting loops bridging over the neutral line. Such a morphology shows up most clearly in two-ribbon flares

Solar Physics **214:** 325–338, 2003.

taking place in spotless regions (cf., Dodson and Hedeman, 1960; Ruždjak *et al.*, 1987, 1989, and references therein). When occurring in a complex magnetic field environment of sunspot groups, the morphology of dynamical flares often happens to be much more intricate due to a number of accompanying energy release events of other types (see, e.g., Aurass *et al.*, 1999).

The energy release in two-ribbon flares is attributed to the reconnection process in a large-scale current sheet formed below the eruptive filament (cf., Priest, 1982)*. The reconnection itself takes place in a tiny diffusion region whose dimensions are determined by the need that the magnetic field inflow has to be balanced by the magnetic diffusion, i.e., that locally the magnetic Reynolds number is $R_M \approx 1$. In the fast reconnection regime the plasma inflows into the sheet at a velocity 1–10% of the ambient Alfvén velocity (cf., Priest, 1982). Such a speed is faster than the slow magnetosonic speed and two pairs of standing slow-mode shocks (SMS) are formed, outlining the two outflowing regions. At SMSs the plasma is heated and the inflow is deflected: The reconnected field lines are strongly bent and the magnetic tension accelerates plasma, creating two hot jets outflowing along the current sheet at a velocity approximately equal to the Alfvén speed in the ambient plasma (e.g., Ugai, 1987a; Aurass, Vršnak, and Mann, 2002). The magnetoplasma outflowing downwards builds a growing system of hot, X-ray emitting flare loops (FL) anchored in the chromospheric flare ribbons (cf., Priest, 1982). FLs cool radiatively, eventually appearing as the cold postflare loops.

In the active region corona the plasma-to-magnetic pressure ratio is low, $\beta \ll 1$, and in such a case the outflowing jets are super-magnetosonic (see, e.g., Skender, Vršnak, and Martinis, 2002, and references therein). At the location where the jet encounters an obstacle, a standing fast-mode shock (FMS) forms. In the two-ribbon flare geometry the jet directed downwards encounters FLs, whereas the one directed upwards meets the bottom of the eruptive filament (see, e.g., Figure 1 in Aurass, Vršnak, and Mann, 2002).

Beside the three basic morphological features of two-ribbon flares (the eruptive filament, the expanding ribbons, and the arcade of flaring loops) several other observational findings support the described two-ribbon flare concept. The most suggestive are the cusped structures seen in soft X-rays (SXR) above the FL system (Tsuneta, 1995, 1998; Aschwanden, 2002). In the region above FLs a superhot, hard X-ray emitting plasma is observed sometimes (Masuda *et al.*, 1994; Uchida *et al.*, 2001)** at the location where FMS is expected (Forbes, 1986; Tsuneta and Naito, 1996). A new important result was recently reported by Yokoyama *et al.*

*Note that in most numerical and analytical studies the flare is modeled independently from the eruptive filament. Sometimes the filament eruption that happens before the current sheet formation is confused with the ejection of the plasmoid which is formed within the current sheet after the reconnection onset. For a self-consistent approach to the problem of filament eruption and the current sheet evolution see, e.g., Martens and Kuin (1989), or Lin and Forbes (2000).

**'Masuda flares' are observed at the limb and were originally classified as simple-loop flares. However, Shibata *et al.* (1995) demonstrated that they in fact belong to dynamical flares and are probably unresolved two-ribbon flares (see also Aschwanden, 2002).

(2001) who performed a detailed analysis of plasma flows above FLs observed by the SXT-instrument aboard the *Yohkoh* satellite. In the studied event they detected plasma motions that could be interpreted as the reconnection inflow. On the other hand, in a number of flares McKenzie and Hudson (1999) and McKenzie (2000) found features moving downwards, presumably belonging to the reconnection outflow. They noticed that the observed velocities are significantly slower than expected in the fast reconnection process (for a discussion see also Klimchuk, 1996; Vršnak, 2003). Recently, Aurass, Vršnak, and Mann (2002) reported observations of a 'non-drifting type II-like burst' in decimetric-to-metric wavelength range and interpreted it as the radio emission from the standing FMS above FLs.

In this paper we present an analysis of the huge quiescent prominence eruption and the spotless two-ribbon flare that took place on 12 September 2000. A relatively simple geometry, large spatial scales, and a suitable viewing angle provide additional information on the characteristics of the energy release process in dynamical flares.

2. Observations

2.1. Data set

The evolution of the Hα flare and the kinematics of the filament are followed utilizing the full-disk Hα filtergrams of the Kanzelhöhe Solar Observatory (Messerotti *et al.*, 1999). Observations are performed in the Hα line center (Figure 1) by a 10-cm aperture refractor equipped with a 0.7 Å FWHM Lyot filter and two digital cameras. We use data from the 1 K $\times$ 1 K 8-bit camera (spatial resolution: 2.3 arc sec per pixel; temporal cadence: $\approx$ 1.5 min) which is operated in a frame selection mode in order to give maximum spatial resolution.

Radio maps in total and circularly polarized brightness were recorded at 432, 411, 327, 237, and 164 MHz by the Nançay Multifrequency Radioheliograph (NRH; Kerdraon and Delouis, 1997). Several examples are shown in Figures 2(a–c) where NRH iso-intensity maps are superposed onto the Hα difference images.

The Hα and NRH data are supplemented by the Fe XII 195 Å full-disk images obtained by the Extreme Ultraviolet Imaging Telescope aboard the Solar and Heliospheric Observatory (EIT-SOHO; Delaboudinière *et al.*, 1995) and the soft X-ray images of the solar corona provided by the *Yohkoh* soft X-ray telescope (SXT; Tsuneta *et al.*, 1991). These supplementary data are used primarily to inspect large scale changes in the corona associated with the eruption and the flare.

2.2. General characteristics of the event

The studied 2N/M1 two-ribbon spotless flare took place in the decaying active region NOAA 9163. It was a dynamical flare associated with the eruption of a

large, more than 350 Mm long, neutral line quiescent filament (Figure 1(a)) and the overlying arcade of intricate structure (Figure 1(b)).

Although it was a large Hα flare with ribbons extending over more than 300 Mm, it caused only a gradual soft X-ray (SXR) burst of modest intensity. It was a long duration event (LDE) with the SXR rise time of almost one hour and the decay lasting for more than five hours (see `http://www.lmsal.com/SXT/plot_goes.html`). In microwaves a gradual rise and fall (GRF) burst was recorded, which is a common characteristic of spotless flares (Ruždjak *et al.*, 1989). At 3 GHz the burst had a rise time of 50 min (11:25–12:15 UT) and peak flux of 150 sfu (*Solar Geophysical Data*: Solar Radio Events, Fixed Frequency).

In late phases of the flare the *Yohkoh* SXT data reveal a relaxed, ≈ 400 Mm long, cusped arcade of hot loops (Figure 1(c)). The flare-associated eruption developed into a fast halo CME that attained a velocity of 1550 km s^{-1}. The constant speed back-extrapolation indicates a lift-off time around 11:40 UT (Yashiro and Michalek, CME catalogue, `http://cdaw.gsfc.nasa.gov/CME_list/`). The CME was accompanied by a traveling MHD shock wave that excited a type II burst extending from the dekameter to the kilometer wavelength range.

2.3. Measurements of positions and kinematics

The filament motion was measured tracing a silhouette of the Hα filament on running difference images. The applied procedure is similar to the one utilized in the analysis of the Moreton wave propagation by Warmuth *et al.* (2001). Radial coordinates of the upper and the lower edge of the filament were determined at 16 position angles between $\phi = 172°$ and $\phi = 209°$, measured from the heliographic north in a counter-clockwise direction. The polar coordinates of a measured element are transformed to obtain the plane-of-sky distances d from the great circle which connects the footpoints of the filament, presumably corresponding to the projected height (h) of the considered element. The distances d are averaged over the position angles of interest and normalized with respect to the solar radius $r_\odot$ to get $D = d/r_\odot$. Assuming that the filament propagated radially, the values of d could be converted to heights by applying the correction for foreshortening as $h = 2.4\,d$, since the midpoint of the line connecting the footpoints of the filament was at the radial coordinate $R = r/r_\odot = 0.42$. Consequently, the radial velocity $v^* = \mathrm{d}h/\mathrm{d}t$ can be estimated from the plane-of-sky velocity $v = \mathrm{d}d/\mathrm{d}t$ utilizing $h = d\,r_\odot/r = d/0.42 = 2.4\,d$, i.e., $v^* = 2.4\,v$.

Locations of radio sources were determined from NRH maps by measuring the cartesian coordinates of the emission maximum (the source 'centroid'). From the (x,y) coordinates the polar coordinates (R,ϕ) are determined, as well as the normalized distances D from the neutral line.

The calibration of NRH position measurements was checked by routine observations of the radio galaxy Cyg A on 8 and 13 September 2000. Only the inner part of the NRH array was used, where the structure of the galaxy is not resolved. The

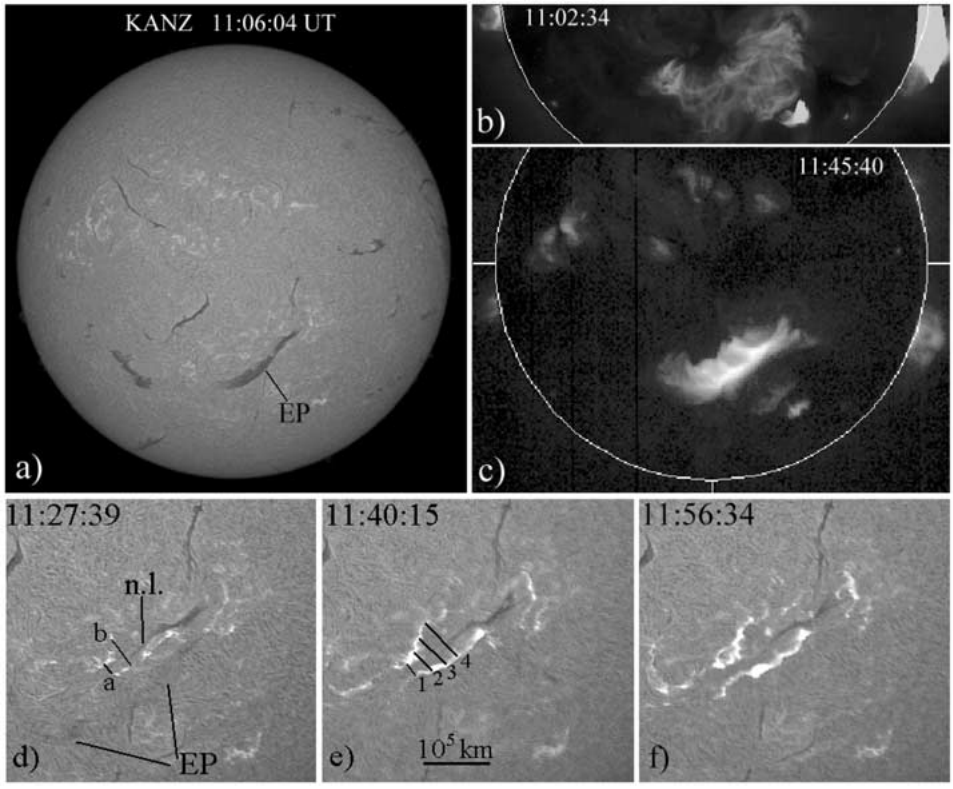

Figure 1. Evolution of the flare: (a) the preflare phase and slow rising motion of the Hα filament; (b) *Yohkoh* SXT image showing the preflare arcade; (c) SXT image revealing cusped arcade of FLs; (d) first Hα brightenings. The neutral line is denoted as n.l. and EP is the eruptive prominence; (e) formation and the onset of expansion of the Hα flare ribbons; (f) the lateral expansion of Hα ribbons. East is left, north is up.

centroid of the source was found at its nominal position to within less than 1 pixel (0.25 arc min) in the interval $\pm$ 2 hours around meridian passage, which covers the interval of hour angles used for the solar observations in this paper.

3. Evolution of the Event

3.1. Development of the flare–filament system

Early stages of the event (Figure 1(a)) showed a common quiescent filament pre-eruption scenario (see, e.g., Vršnak, 1992). The eruption was preceded by enhanced internal motions, swelling, and a slow rise of the filament. A particular onset time cannot be specified since the filament was showing internal activity already at 06:30 UT when the Hα observations started. Helical-like elements within the filament could be recognized around 11 UT. At this time the plane-of-sky velocity

was still less than 1 km s^{-1}, and the distance from the frontal (upper) edge of the filament to the neutral line was $d_U = 80$ Mm. Assuming that the plane of the filament was normal to the solar surface the corresponding height is estimated to be $h_U \approx 190$ Mm.

The SXR burst started very gradually between 11:20 and 11:25 UT. Approximately at the same time the first signs of radio activity in the vicinity of the filament were recorded by NRH (Figure 3). The intensity of bursts and their occurrence rate was successively increasing. The Hα point-like brightenings appeared at both sides of the neutral line. The closest ones were separated by $w = 20$–25 Mm (line 'a' in Figure 1(d)), but at some locations the distance was up to ≈ 50 Mm (line 'b' in Figure 1(d)). The projected distance from the neutral line to the lower edge of the filament was $d_L = 50$ Mm which corresponds to the height of $h_L \approx 120$ Mm. The filament upper edge reached the height of $h_U \approx 300$ Mm having a heliocentric velocity of $v_U^* \approx 100$ km s^{-1}.

The formation of the Hα ribbons was completed and the lateral expansion started at 11:40 UT. The velocity depended on the location along the neutral line and amounted to $dw/dt \approx 10$–15 km s^{-1} at the beginning of the expansion. Some parts of the ribbons remained stationary. At the onset of the ribbon expansion the lower edge of the filament was already at $d_L = 150$ Mm away from the neutral line (Figure 4) which corresponds to the height of $h_L \approx 360$ Mm. Simultaneously, the ribbon separation measured perpendicular to the neutral line at the expanding parts of ribbons, was $w = 20$–40 Mm (lines '1' and '2' in Figure 1(e)), which corresponds to the w/h ratio $\frac{1}{18}$–$\frac{1}{9}$. The largest separation of the ribbon elements was up to 60–75 Mm, corresponding to the w/h ratio $\frac{1}{6}$–$\frac{1}{5}$. We emphasize that these values are measured along the two lines denoted as '3' and '4' in Figure 1(e), connecting the elements of ribbons which did not show any lateral expansion at this stage.

The Hα filament and its EIT 195 Å counterpart were not traceable after 11:48 UT. The last measured (projected) speed of the leading edge was $v_U = 320$ km s^{-1}. The 2nd degree polynomial fit to the leading edge data $d(t)$ in the period 11:20–11:48 UT gives for the average plane of sky acceleration $\overline{a}_U \approx 200$ m s^{-2}. It should be noted that the corresponding value of the heliocentric acceleration, $a^* \approx 480$ m s^{-2}, is quite large for eruptive prominences (St. Cyr *et al.*, 1999; Vršnak, 2001).

The SXR burst attained a broad maximum at around 12:13 UT, roughly corresponding to the maximum of the Hα flare (see the two horizontal arrows in Figure 4(a)).

The radio event seen by the NRH started with two adjacent sources (referred to as A and B in Figure 2(d)) which were elongated in the general direction of the pre-eruptive filament. The two source regions were clearly separated by the filament. A moving type IV radio burst developed out of region A ahead of the filament (432 to 237 MHz, 11:30–11:42 UT). The sources at different frequencies are found at slightly different positions. As a whole, they outline a curved columnar structure

anchored near the south-eastern extremity of the filament. This structure moved gradually westward until 11:40 UT, that is the time when the Hα ribbons started to drift apart. At this time the emission at 432 and 411 MHz faded, and the structure outlined by the sources at 327 and 237 MHz started moving radially outward at position angle 216°. The 164 MHz emission shows a somewhat different behavior, including bursts which have no counterpart at higher frequencies. A snapshot displaying three sources that brightened in succession during this period is shown in Figure 2(c).

During the moving type IV burst various sources brightened in the complex B behind the filament (Figure 2(d)), randomly bursting at different positions all over the area bounded by the lower edge of the filament and the neutral line. Several groups of broadband brightenings occurred until 13:30 UT. As will be shown below, the outer limit of the complex B was rising together with the filament, overlapping with the lower edge of its silhouette. In the following we focus on source B, which we presume to represent radio emission related to the current sheet below the erupting filament. The locations of sources B, and a roughly contemporaneous silhouette of the filament are shown for two time intervals in Figures 3(a) and 3(b).

3.2. Locations of radio sources

The radio emission from the region below the eruptive filament (sources B) was characterized by an apparently random occurrence of impulsive bursts. The bursts were often recorded only at one of the observing frequencies (Figures 3 and 4(a)). Most of the source centroids were located near the lower edge of the filament, closely following its rising motion (Figure 3). This is illustrated more clearly by Figure 4 where the projected normalized distances $D(t)$ of the lower and upper filament edge, averaged over the sector $\phi = 172° - 189°$, are compared with the distances of the centroids of radio sources B.

In Figure 4(a) the sources are sorted by the emission frequency. In Figure 4(b) they are provisionally separated into three groups, following the impression that they represent distinct groups of sources with respect to the projected distance from the neutral line. The groups are denoted as B1, B2, and B3, and are drawn in Figure 4(b) by squares, triangles, and circles, respectively. The occurrence rate of the low-lying sources B1 and the mid-height sources B2 was considerably smaller than the occurrence rate of sources B3. No preferred position along the neutral line could be recognized.

Figure 4(a) shows no distinct relationship between the source location and the emission frequency – each frequency can be found at any position. There is only a weak tendency of lower frequencies to appear at larger distances from the neutral line, i.e., at larger heights.

The radio-emitting region was spreading in the south-west direction till $\approx$ 11:50 UT. The sources most distant from the neutral line were recorded at 327 MHz at $d = 200$ Mm, corresponding to a height of $h \approx 480$ Mm. After

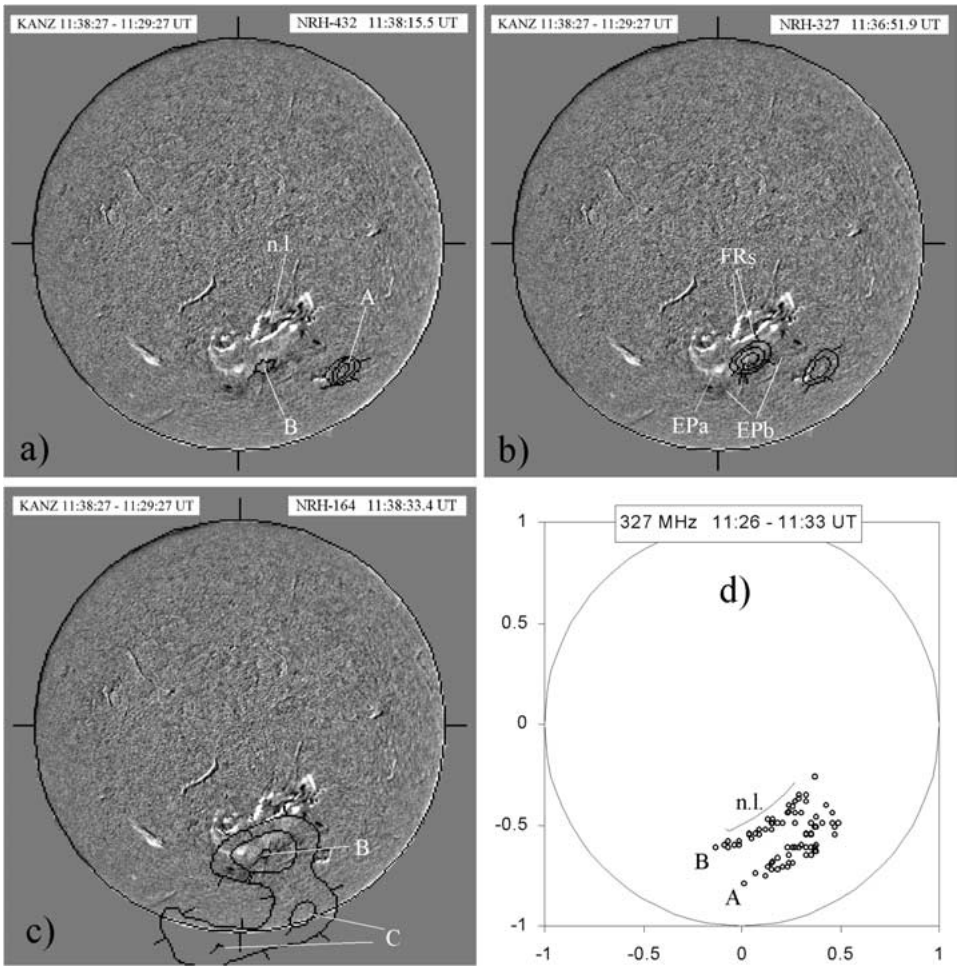

Figure 2. (a)–(c) Three NRH iso-intensity maps superposed onto the Hα difference image (11:38:27 – 11:29:27 UT). The neutral line and the flare ribbons are denoted as n.l. and FRs, respectively. The eruptive prominence at 11:29:27 UT is seen as a white silhouette (EPa), and at 11:38:27 UT as a black silhouette (EPb). The NRH maps show examples of sources A, B, and C at 432 MHz (a), 327 MHz (b), and 164 MHz (c). (d) Centroids of the most prominent radio bursts in the period 11:26 – 11:33 UT. The sources ahead of the filament (moving type IV burst) are denoted as A, and those below the filament as B.

12 UT only the sources B1 and B2 were observed (Figure 4(b)), whereas those following the lower edge of the filament were not found anymore.

The increasing distances $d(t)$ of sources B1, B2, and B3 are fitted by 2nd degree polynomials (Figure 4(b)). The plane-of-sky velocities at the onset of the radio activity ($\approx$11:26 UT) are estimated to be $v_1 \approx 20$ km s^{-1}, $v_2 \approx 50$ km s^{-1},

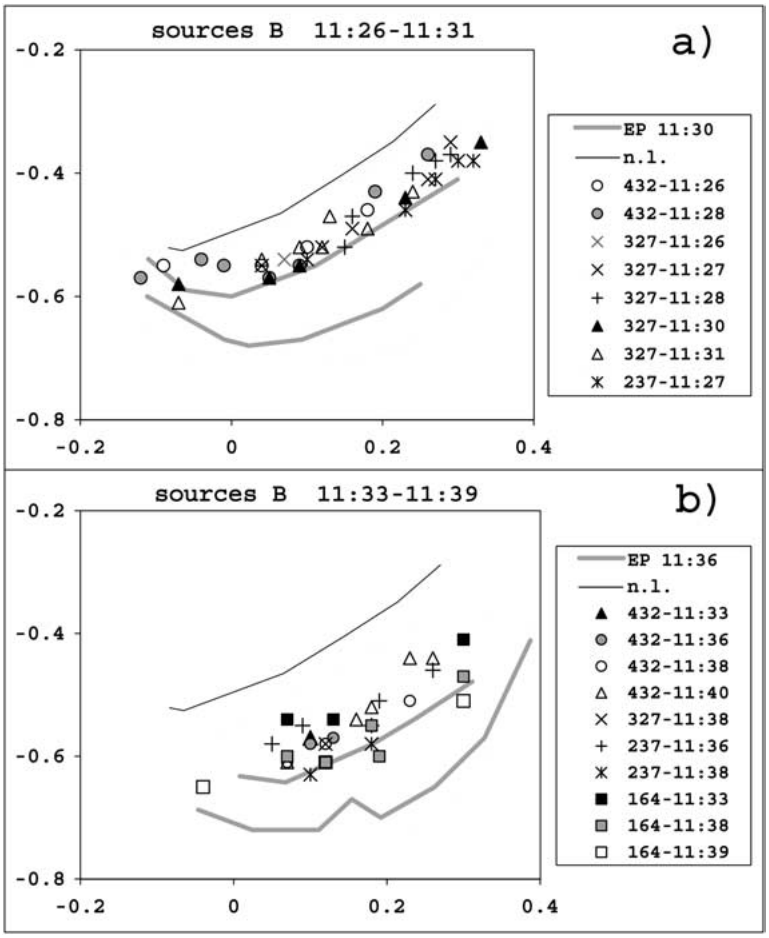

Figure 3. (a) Positions of centroids of radio bursts B in the period 11:26–11:31 UT. The filament contours at 11:30 UT are drawn by *thick gray lines*. The neutral line is marked by a *thin black line*. (b) The same as in (a) but for the period 11:33–11:40 UT and filament contours at 11:38 UT. The axes are graded in fractions of a solar radius. The observing frequencies and times are specified in the legend.

and $v_3 \approx 100$ km s^{-1}, respectively*. The corresponding values corrected for the projection effects are 50, 120, and 240 km s^{-1}, respectively.

4. Interpretation and Discussion

The described event shows all the essential features of an ordinary two-ribbon flare. It is similar to the one discussed by Klein and Mouradian (2002). A relatively

*The data point drawn in Figure 4b by a small circle is not taken into account in the fitting since it is not clear to which group, B2 or B3, it should be attributed.

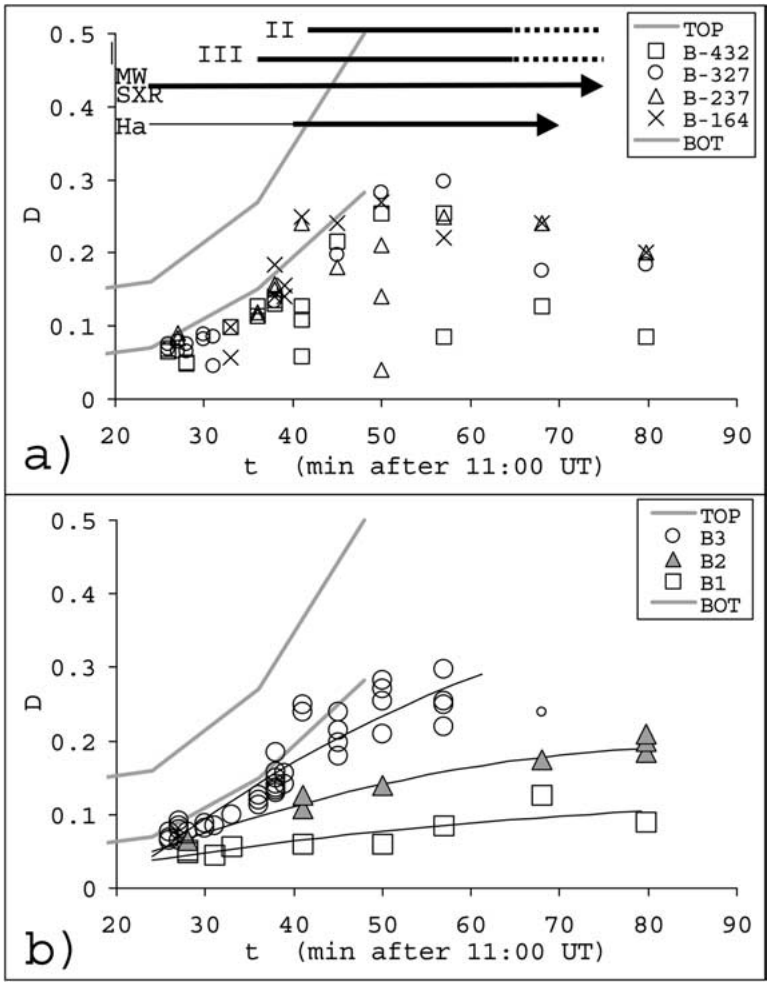

Figure 4. (a) The normalized distance ($D = d/r_{\odot}$) of the radio sources B from the neutral line as observed at different frequencies. The upper and the lower edge of the filament are shown by *gray lines*. The *horizontal arrows* show the rising phase of the microwave burst (MW), soft X-ray burst (SXR), and Hα flare (arrow indicates the time of maximum). The *thinner part* of the Hα arrow represents stationary brightenings of fluctuating intensity observed prior to the formation of flare ribbons. The timing of the metric type II burst and group of type III burst is indicated by the other two *bold horizontal lines*. (b) Sources B are separated provisionally into three groups. The fitted 2nd degree polynomials are shown by *thin lines.*

simple flare geometry, large spatial scales, and a suitable viewing angle allowed us to determine the relative position of the eruptive filament, the flare ribbons, and the flare radio emission. In the following we discuss these observations in the context of the two-ribbon flare model, to clarify some characteristics of the energy release process in dynamical flares.

First we emphasize two aspects which we find especially important:

– the ratio of the ribbon separation and the height of the lower edge of the filament, estimated for the expanding parts of ribbons, was $\frac{1}{18}-\frac{1}{9}$ at the onset of the expansion; the elements with $w/h > \frac{1}{6}$ remained stationary;

– with the exception of the moving type IV burst, radio sources occurred preferentially close to the lower edge of the filament and some are observed at relatively low heights ($h \approx 0.1\, r_\odot$) above the magnetic inversion line.

Adopting the standard concept of a two-ribbon flare (see, e.g., Figure 1 in Aurass, Vršnak, and Mann, 2002) it is reasonable to assume that the emission confined to the region between the neutral line and the lower edge of the filament (sources B) is excited in the current sheet formed below the eruptive filament. The current sheet is the site of the fast magnetic reconnection which is shown by the lateral expansion of the flare ribbons.

Let us first summarize some aspects of the two-ribbon flare model which should be kept in mind when interpreting the observations.

Since the preflare magnetic arcade is sheared, the current sheet formed behind the rising filament initially has a substantial transversal component of the magnetic field $B_x \neq 0$ (see, e.g., Aschwanden, 2002; Vršnak, 2003, and references therein)*. The presence of B_x hinders a high energy release rate, and on the other hand, allows compression in the current sheet larger than in the $B_x = 0$ case (Soward, 1982, see also Skender, Vršnak, and Martinis, 2002, and references therein). As the filament rises the field lines are stretched, so the ratio of the transversal component B_x and the vertical B_z component decreases.

Another parameter relevant for the onset of fast reconnection is the width-to-length ratio of the current sheet, δ/λ: the fast reconnection can start only after λ becomes considerably larger than δ (Ugai, 1987b). Since the current sheet elongates as the filament rises (Martens and Kuin, 1989; Lin and Forbes, 2000), the ratio δ/λ decreases.

4.1. THE ONSET OF FAST RECONNECTION

The flare started gradually by a weak energy release, indicated by the appearance of low-intensity Hα brightenings and a slowly enhancing SXR emission. The lower edge of the filament in this stage reached the height $h_L \approx 120$ Mm. Since the distance between the Hα brightenings across the neutral line was not smaller than $w = 20$ Mm, the current sheet width-to-length ratio could not be smaller than $\delta/\lambda \approx w/h_L = \frac{1}{6}$. This value is still too large for the onset of fast reconnection in the current sheet (Ugai, 1987b). Indeed, no lateral expansion of the Hα ribbons was observed at this stage.

We see two feasible mechanisms governing this early phase of the energy release. One possibility is that an internal restructuring in a form of loop interaction took place within the sheared arcade before the two-ribbon phase. Such an event,

*The horizontal axes x and y are oriented parallel and perpendicular to the magnetic inversion line, respectively, whereas the z axis is oriented vertically.

having signatures of a compact flare and setting-on the two-ribbon flare of 25 October 1994 was reported by Aurass *et al.* (1999) and discussed by Vršnak (2003).

On the other hand, it is also possible that the early energy release is a consequence of the reconnection that was *driven* by converging flows formed behind the erupting filament (for the flow patterns generated in the ambient magnetoplasma by a moving flux rope see numerical simulations by Cargill *et al.*, 1995, 1996). The ratio of the transverse and the antiparallel field component (B_x/B_z) was still too high to allow a fast energy release. However, already at a comparatively slow merging velocity, plasma instabilities could be triggered in the current sheet (Vršnak, 1989) resulting in the radio emission. Since vortices behind the filament are turbulent, one can expect a variable inflow velocity causing a fluctuating energy release rate. Indeed, the early Hα brightenings were showing fluctuating intensity.

According to the standard two-ribbon flare model the lateral expansion of Hα ribbons is a signature of fast reconnection in the current sheet below the filament. This process started at 11:40 UT when the width-to-length ratio of the current sheet decreased to the value between $\frac{1}{18}$ and $\frac{1}{5}$. As stressed in Section 3.1, the latter value was measured at the location where the ribbons were still not expanding. The *expanding parts* were characterized by the w/h ratio between $\frac{1}{18}$ and $\frac{1}{9}$, which is in fairly good agreement with the threshold value for the onset of the tearing instability $\delta/\lambda \approx \frac{1}{15}$ (Ugai, 1987b).

4.2. THE RADIO EMISSION

The position of the radio sources suggests that the emitting electrons are accelerated in the reconnecting current sheet below the erupting filament or in its neighborhood. In the fast reconnection process the velocity of the plasma outflowing from the current sheet is generally super-magnetosonic, not depending much on the inflow speed (for details see Skender, Vršnak, and Martinis, 2002, and references therein). At the location where the super-magnetosonic flow meets an obstacle the standing fast-mode shock (FMS) is formed. In the two-ribbon flare configuration this should presumably happen above the flaring loops (Forbes, 1986; Somov and Kosugi, 1997; Tsuneta and Naito, 1996) and at the lower edge of the filament (Magara *et al.*, 2000). Figure 4 shows that the radio bursts in the studied event occurred preferentially at the lower edge of the filament, but some are observed also at low heights around $h \approx 0.1\, r_\odot$. Bearing in mind the event reported by Aurass, Vršnak, and Mann (2002), it is tempting to attribute the observed emission to FMSs. However, we note that turbulence at the interface between the outflow and the ambient plasma will create waves that are also potential accelerators, even if the outflow is not super-magnetosonic.

Yet, at least one more explanation is possible. For example, when the current sheet becomes long enough, two or more X-type neutral lines can appear in the sheet, causing the formation of 'magnetic islands', sometimes also called plasmoids (Biskamp, 1982; Forbes and Priest, 1983; see also, e.g., Magara *et al.*, 1996,

and references therein; for laboratory experiments see, e.g., Gekelman and Pfister, 1988). Numerical simulations show that plasmoids should be ejected preferentially upwards (e.g., Magara *et al.*, 1996), but sometimes downward moving ones are observed too (Forbes and Priest, 1983; for the 3-D aspect see Vršnak, 2003). The coalescence of the plasmoids ejected upwards with the lower boundary of the erupting flux rope imbedding the filament might be an alternative cause of the sources B3. Similarly, the plasmoids ejected downwards might cause the radio emission B1 when interacting with the flaring loops (Forbes and Priest, 1983). In such a scenario, the mutual plasmoid coalescence (see e.g., Tajima *et al.*, 1987; Schumacher and Kliem, 1997) would be the cause of B2 bursts.

Note that the interpretation in terms of plasmoid formation, ejection, and coalescence explains straightforwardly the intermittent nature of the radio emission (Kliem, 1995). A possible explanation of the intermittence in the case of the FMS-scenario is discussed by Klimchuk (1996) and Vršnak (2003). On the other hand, it is difficult to explain the early radio emission in terms of the coalescence scenario, since in this phase the current sheet was still relatively short and not suitable for multiple tearing.

Acknowledgements

We would like to thank the SOHO, *Yohkoh*, and GOES teams for developing and operating the instruments and for the open data policy, and the Center for Solar Physics and Space Weather, The Catholic University of America, for providing its CME catalog in cooperation with the Naval Research Laboratory and NASA. The Nançay Radio Observatory is funded by the French Ministry of Education, the CNRS and the Région Centre. B.V. is grateful for the hospitality he experienced during his stay in Meudon at DASOP – Observatoire de Paris and acknowledges the financial support by CNRS.

References

Aschwanden, M. J.: 2002, *Space Sci. Rev.* **101**, 1.
Aurass, H., Vršnak, B., and Mann, G.: 2002, *Astron. Astrophys.* **384**, 273.
Aurass, H., Vršnak, B., Hofmann, A., and Ruždjak, V.: 1999, *Solar Phys.* **190**, 267.
Biskamp, D.: 1982, *Phys. Lett.* **87A**, 357.
Cargill, P. J., Chen, J., Spicer, D. S., and Zalesak, S. T.: 1995, *Geophys. Res. Lett.* **22**, 647.
Cargill, P. J., Chen, J., Spicer, D. S., and Zalesak, S. T.: 1996, *J. Geophys. Res.* **101**, 4855.
Delaboudinière, J.-P., Artzner, G. E., Brunaud, J. *et al.*: 1995, *Solar Phys.* **162**, 291.
Dodson, H. W. and Hedeman, E. R.: 1960, *Astron. J.* **65**, 51.
Forbes, T. G.: 1986, *Astrophys. J.* **305**, 553.
Forbes, T. G. and Priest, E. R.: 1983, *Solar Phys.* **84**, 169.
Gekelman, W. and Pfister, H.: 1988, *Phys. Fluids*, **31**, 2017.

Kerdraon, A. and Delouis, J.: 1997, in G. Trottet (ed.), *Coronal Physics from Radio and Space Observations*, Springer-Verlag, Heidelberg, p. 192.
Klein, K.-L. and Mouradian, Z.: 2002, *Astron. Astrophys.* **381**, 683.
Kliem, B.: 1995, *Lecture Notes of Physics* **444**, 93.
Klimchuk J. A.: 1996, *ASP Conf. Series* **111**, 319.
Lin, J. and Forbes, T. G.: 2000, *J. Geophys. Res.* **105**, 2375.
Magara, T., Mineshige, S., Yokoyama, T., and Shibata, K.: 1996, *Astrophys. J.* **466**, 1054.
Magara, T., Chen, P., Shibata, K., and Yokoyama, T.: 2000, *Astrophys. J.* **538**, L175.
Martens, P. C. H. and Kuin, N. P. M.: 1989, *Solar Phys.* **122**, 263.
Masuda, S., Kosugi, T., Hara, H., Tsuneta, S., and Ogawa, Y.: 1994, *Nature* **371**, 495.
McKenzie, D. E.: 2000, *Solar Phys.* **195**, 381.
McKenzie, D. E. and Hudson, H. S.: 1999, *Astrophys. J.* **519**, L93.
Messerotti, M., Otruba, W., Warmuth, A. *et al.*: 1999, in N. Crosby (ed.), *Proc. ESA Workshop on Space Weather*, WPP-155; ESA, Noordwijk, p. 321.
Priest, E. R.: 1982, *Solar Magnetohydrodynamics*, D. Reidel Publ. Co., Dordrecht, Holland.
Ruždjak, V., Messerotti, M., Nonino, M., Schroll, A., Vršnak, B., and Zlobec, P.: 1987, *Solar Phys.* **111**, 103.
Ruždjak, V., Vršnak, B., Schroll, A., and Brajša, R.: 1989, *Solar Phys.* **123**, 309.
Schumacher, J. and Kliem, B.: 1997, *Phys. Plasmas* **4**, 3533.
Shibata, K., Masuda , S., Shimojo, M. *et al.*: 1995, *Astrophys. J.* **451**, L83.
Somov, B. V. and Kosugi, T.: 1997, *Astrophys. J.* **485**, 859.
Soward, A. M.: 1982, *J. Plasma Phys.* **28**, 415.
Skender, M., Vršnak, B., and Martinis, M.: 2002, *Proc. 10th European Solar Phys. Meeting*, Prague 9–14 September 2002, ESA SP-506, p. 757.
St. Cyr, O. C., Howard, R. A., Sheeley, N. R. *et al.*: 1999, *J. Geophys. Res.* **104**, 12493.
Švestka, Z.: 1976, *Solar Flares*, D. Reidel Publ. Co., Dordrecht, Holland.
Tajima, T., Sakai, J., Nakajima, H., Kosugi, T., Brunel, F., and Kundu, M. R.: 1987, *Astrophys. J.* **321**, 1031.
Tsuneta, S.: 1995, *Publ. Astron. Soc. Japan* **47**, 691.
Tsuneta, S.: 1996, *Astrophys. J.* **456**, 840.
Tsuneta, S. and Naito, T.: 1998, *Astrophys. J.* **495**, L67.
Tsuneta, S., Acton, L., Bruner, M. *et al.*: 1991, *Solar Phys.* **136**, 37.
Uchida, Y., Wheatland, M. S., Haga, R., Yoshitake, I., and Melrose, D.: 2001, *Solar Phys.* **202**, 117.
Ugai, M.: 1987a, *Geophys. Res. Lett.* **14**, 103.
Ugai, M.: 1987b, *Phys. Fluids* **30**, 2163.
Vršnak, B.: 1989, *Solar Phys.* **120**, 79.
Vršnak, B.: 1992, *Ann. Geophys.* **10**, 344.
Vršnak, B.: 2001, *J. Geophys. Res.* **106**, 25249.
Vršnak, B.: 2003, *Lecture Notes of Physics* **612**, 28.
Warmuth, A., Vršnak, B., Aurass, H., and Hanslmeier, A.: 2001, *Astrophys. J.* **560**, L105.
Yokoyama, T., Akita, K., Morimoto, T., Inoue, K., and Newmark, J.: 2001, *Astrophys. J.* **546**, L69.